AGU PUBLICATIONS

JGR

Journal of Geophysical Research: Atmospheres

RESEARCH ARTICLE
10.1002/2013JD020627

Special Section:
The Geoengineering Model Intercomparison Project (GeoMIP)

Key Points:
- Sea ice extents decrease despite sulfate aerosol injection
- Ice extents collapse back to RCP4.5 levels after geoengineering stops
- Negative net radiative forcing is necessary to stop snow/sea ice melting

Correspondence to:
M. Berdahl,
mberdahl@envsci.rutgers.edu

Citation:
Berdahl, M., A. Robock, D. Ji, J. C. Moore, A. Jones, B. Kravitz, and S. Watanabe (2014), Arctic cryosphere response in the Geoengineering Model Intercomparison Project G3 and G4 scenarios, *J. Geophys. Res. Atmos.*, *119*, 1308–1321, doi:10.1002/2013JD020627.

Received 26 JUL 2013
Accepted 2 JAN 2014
Accepted article online 5 JAN 2014
Published online 15 FEB 2014

Arctic cryosphere response in the Geoengineering Model Intercomparison Project G3 and G4 scenarios

Mira Berdahl[1], Alan Robock[1], Duoying Ji[2], John C. Moore[2], Andy Jones[3], Ben Kravitz[4], and Shingo Watanabe[5]

[1]Department of Environmental Sciences, Rutgers University, New Brunswick, New Jersey, USA, [2]State Key Laboratory of Earth Surface Processes and Resource Ecology, College of Global Change and Earth System Science, Beijing Normal University, Beijing, China, [3]Met Office Hadley Centre, Exeter, UK, [4]Atmospheric Sciences and Global Change Division, Pacific Northwest National Laboratory, Richland, Washington, USA, [5]Japan Agency for Marine-Earth Science and Technology, Yokohama, Japan

Abstract We analyzed output from the Geoengineering Model Intercomparison Project for the two most "realistic" scenarios, which use the representative concentration pathway of 4.5 Wm^{-2} by 2100 (RCP4.5) as the control run and inject sulfate aerosol precursors into the stratosphere. The first experiment, G3, is specified to keep RCP4.5 top of atmosphere net radiation at 2020 values by injection of sulfate aerosols, and the second, G4, injects 5 Tg SO_2 per year. We ask whether geoengineering by injection of sulfate aerosols into the lower stratosphere from the years 2020 to 2070 is able to prevent the demise of Northern Hemispere minimum annual sea ice extent or slow spring Northern Hemispere snow cover loss. We show that in all available models, despite geoengineering efforts, September sea ice extents still decrease from 2020 to 2070, although not as quickly as in RCP4.5. In two of five models, total September ice loss occurs before 2060. Spring snow extent is increased from 2020 to 2070 compared to RCP4.5 although there is still a negative trend in 3 of 4 models. Because of the climate system lag in responding to the existing radiative forcing, to stop Arctic sea ice and snow from continuing to melt, the imposed forcing would have to be large enough to also counteract the existing radiative imbalance. After the cessation of sulfate aerosol injection in 2070, the climate system rebounds to the warmer RCP4.5 state quickly, and thus, any sea ice or snow retention as a result of geoengineering is lost within a decade.

1. Introduction

The Arctic has been warming twice as quickly as the global average in recent decades [e.g., *Serreze and Francis*, 2006; *Solomon et al*., 2007] and three times as quickly as the average of all other nonpolar regions of the world [*Ahmed et al*., 2013]—a characteristic known as Arctic amplification. One of the major concerns associated with such extreme rates of warming is the demise of Arctic sea ice. All monthly extents of Arctic sea ice have declined over the period of observations, most rapidly for September [*Serreze et al*., 2007, http://nsidc.org/arcticseaicenews/]. This decline has been shown to be congruent with strong surface warming [*Screen and Simmonds*, 2010]. For example, *Tingley and Huybers* [2013] showed that the summers of 2005, 2007, 2010, and 2011 were warmer than those of all prior years back to 1400 in the high northern latitudes. These years are also associated with record minimum sea ice extents [*National Snow and Ice Data Center*, 2012]. *Serreze et al*. [2009] and *Screen and Simmonds* [2010] demonstrated that strong positive ice-temperature feedbacks have already emerged in the Arctic, increasing the chances of further warming and ice loss. The Coupled Model Intercomparison Project (CMIP5) models vary in estimates for when ice-free conditions will occur, some predicting as early as 2020 [*Stroeve et al*., 2012; *Wang and Overland*, 2012]. *Stroeve et al*. [2012] found that, even with the same emissions scenario, there is a large scatter between different model simulations (both between different models and between ensemble members from the same model) as to the timing of a seasonally ice-free Arctic Ocean. Under the same emissions scenario, models project this could occur as early as 2020 or well beyond 2100. Uncertainty in future greenhouse gas emissions leads to further uncertainty regarding when ice-free conditions will occur.

Along with the rapid deterioration of Arctic sea ice, Arctic snow cover on land has also been quickly receding over the past several decades. *Derksen and Brown* [2012] found statistically significant reductions in May and

June Arctic snow cover extent from 1967 to 2012. They also noted that the rate of June snow cover loss between 1979 and 2011 is greater than the loss of September sea ice extent over the same period, emphasizing the gravity of the observed changes. As with sea ice, *Brown and Robinson* [2011] showed that significant reductions observed in the Northern Hemisphere spring snow cover extent over the past 90 years are mainly driven by warmer temperatures. Projections for future spring snow cover duration suggest a decrease by about 10–20% over much of the Arctic by the year 2050 [*Callaghan et al*., 2011].

Observed changes in the Arctic could have further reaching implications than just physical effects. Losses in Arctic sea ice and earlier snow melt on high-latitude land have been linked to more persistent midlatitude weather patterns, which may lead to an increased probability of extreme weather events [*Francis and Vavrus*, 2012]. Further, the permanent loss of permafrost and increases in active layer thickness have consequences not only for transportation and the livelihood of high-latitude communities, but also the thaw and release of carbon from the ground can amplify surface warming and initiate a positive permafrost carbon feedback on climate [*Schaefer et al*., 2011].

Geoengineering has been proposed in recent literature as a way to curb global warming and reduce some of the risks associated therein [e.g., *Launder and Thompson*, 2009]. *Crutzen* [2006] suggested that artificial reduction of incoming solar radiation, called solar radiation management (SRM) [*Lane et al*., 2007], could be a means of offsetting the effects of increasing greenhouse gas concentrations by reducing solar absorption [*Shepherd et al*., 2009]. Several SRM approaches have been suggested, but *Lenton and Vaughan* [2009] contend that among the most effective would be by stratospheric aerosol injection. The possible regional effects of such a scenario are still uncertain. *Robock et al*. [2008, 2009] and *Tilmes et al*. [2008] identify the possibility of unintended consequences such as ozone depletion and disruptions to the global hydrologic cycle. Although large volcanic eruptions show winter warming over the Northern Hemisphere continents, a dynamical response to stratospheric heating, *Robock et al*. [2008] did not find such responses in their simulations of sulfate aerosol geoengineering. This is because with geoengineering the stratospheric aerosol distribution would be more uniform, not producing the gradients that drive this circulation response. It is thus of paramount interest to assess the effects of geoengineering on the Arctic, given its high sensitivity to increases in greenhouse gases and the weighty consequences of continued warming.

Previous work on the effects of geoengineering showed warmer poles and cooler tropics with respect to preindustrial conditions [*Lunt et al*., 2008; *Govindasamy and Caldeira*, 2000; *Matthews and Caldeira*, 2007]. Yet certain geoengineering scenarios produce a reduction in the melt of sea ice [*Kravitz et al*., 2013] and ice sheets [*Irvine et al*., 2009] compared to the preindustrial. These inconclusive results, partly due to differing experiments and models, spurred the Geoengineering Model Intercomparison Project (GeoMIP) [*Kravitz et al*., 2011a]. GeoMIP constitutes a suite of four SRM experiments, aimed at understanding how geoengineering might offset climate change projected in some of the CMIP5 experiments.

In this paper we analyze the results from the geoengineering experiments G3 and G4. Of the four GeoMIP experiments, G3 and G4 represent the more "realistic" scenarios in that they use the RCP4.5 (representative concentration pathway, with a radiative forcing of 4.5 Wm^{-2} in the year 2100) [*Moss et al*., 2010] global warming scenario as the control run, and they model stratospheric aerosol injection rather than insolation reduction. Whereas G1 and G2 balance top of atmosphere radiation by reducing the solar constant to a lower value, the G3 experiment adds stratospheric aerosol gradually to the lower stratosphere. Prior to GeoMIP, only a handful of independent studies using general circulation models have simulated SRM scenarios by injection of SO_2 into the lower stratosphere [*Robock et al*., 2008; *Rasch et al*., 2008; *Jones et al*., 2010; *Niemeier et al*., 2011].

G3 injects sulfate aerosols beginning in 2020 to balance the anthropogenic forcing and attempt to keep the net forcing constant (at 2020 levels) at the top of the atmosphere [*Kravitz et al*., 2011a]. The G4 experiment is similar to G3 in simulating a stratospheric sulfate layer beginning in 2020, but it does not attempt radiative balance with anthropogenic emissions. Rather, it injects stratospheric aerosols at a rate of 5 Tg SO_2 per year to effectively delay global warming by about 40 years [*Kravitz et al*., 2011a]. This may be compared with the 20 Tg of SO_2 injected into the stratosphere by the 1991 eruption of Mount Pinatubo [*Robock et al*., 2008; *Bluth et al*., 1992]. Both G3 and G4 cease sulfate aerosol injection in 2070, and the models then continue from 2070 for at least 20 more years, such that the post-engineered rebound of the climate system can be assessed. Large volcanic eruptions that inject sulfate aerosols into the stratosphere with an *e*-folding decay time of

Table 1. Models Participating in GeoMIP That Have Thus Far Run the G3 and G4 Experiments and Number of Ensemble Members Simulated for Each Group

Models in G3	Models in G4	Ensemble Members
BNU-ESM *Dai et al.* [2003, 2004]	BNU-ESM *Dai et al.* [2003, 2004]	1
GISS-E2-R *Schmidt et al.* [2006]	GISS-E2-R *Schmidt et al.* [2006]	3
HadGEM2-ES *Collins et al.* [2011]	HadGEM2-ES *Collins et al.* [2011]	3
	MIROC-ESM *Watanabe et al.* [2011]	1
	MIROC-ESM-CHEM *Watanabe et al.* [2011]	1

approximately 1 year [e.g. *Barnes and Hoffman*, 1997] can cause global cooling for up 2 or 3 years [*Robock*, 2000]. Similarly short aerosol lifetimes are expected with the G3 and G4 sulfate injections, meaning, a sudden suspension of SRM will cause a rapid rebound in the climate. Whereas in G2 the forcing disappears immediately when insolation is returned to the control value, in G3 and G4 there is a delay of 1–2 years as the aerosol forcing gradually disappears. For a more technical overview of GeoMIP experiment specifications, refer to *Kravitz et al*. [2011b]. By using the G3 and G4 experiments of GeoMIP to assess impacts on the Arctic, we benefit from a multimodel and multiexperiment comparison, each model having consistent inputs and parameters, and two unique sulfate aerosol experiments.

We ask how much the Arctic would cool in the G3 and G4 scenarios, and whether geoengineering in a higher CO_2 world would prevent the demise of multiyear sea ice. We also examine the effects of geoengineering on the already decreasing Arctic spring snow cover on land. Furthermore, we examine the post-geoengineering period (after 2070) to see how the Arctic cryosphere rebounds after the cessation of aerosol injection deemed the "Termination Effect" [e.g., *Wigley*, 2006; *Jones et al*., 2013]. Section 2 describes the methods and data sets used, section 3 describes our results, section 4 presents a summary, and section 5 some discussion and conclusions.

2. Methods

Modeling groups that participated in each experiment (G3 and G4) and that are reported in this paper are summarized in Table 1. The MIROC-ESM and MIROC-ESM-CHEM models are treated separately since they branch from unique control runs and include different processes. MIROC-ESM-CHEM includes an online chemistry module that predicts atmospheric ozone and other major chemical species. The GISS-E2-R and HadGEM2-ES modeling groups ran three ensemble members, and all results reported here show their ensemble mean. The other models generated one ensemble member.

The observational data we use for comparison to global and Arctic near surface temperatures are the 2 m gridded temperatures from the latest European Centre for Medium-Range Weather Forecasts (ECMWF) Re-Analysis, ERA-Interim [*Dee et al*., 2011], available from 1979 to present. The data were obtained from the ECMWF Data Server. ERA-Interim is considered to have more accurate estimates of surface temperature in the polar regions [*Jones and Harpham*, 2013] than its predecessor, ERA-40 [*Uppala et al*., 2005].

Monthly mean Arctic sea ice extents, generated from passive microwave satellite data, were downloaded from the National Snow and Ice Data Center (NSIDC) [*Fetterer et al*., 2009]. The data are available from 1979 to present and use a 15% monthly mean concentration threshold for determining ice extent [*Serreze et al*., 2007].

Snow cover data were obtained from the Rutgers University Global Snow Lab (accessible from http://snowcover.org). We used monthly Northern Hemisphere snow extent values from 1967 to 2012. The grid cells are considered fully snow covered if they have at least 50% fractional snow cover; otherwise, they are considered snow free.

In our analyses we computed area-weighted averages of the Arctic (60–90°N unless otherwise noted) temperature, sea ice, and snow. Sea ice extent is defined as grid cells containing $\geq$ 15% concentration, as is standard per NSIDC data. We define grid cells as snow covered if they have at least 50% fractional snow cover, as per standard practice at NSIDC and the Rutgers Snow Lab. In the snow calculations for the GISS-E2-R model, we add to the CMIP5 RCP4.5 curve the anomaly of the geoengineering experiments with respect to the GeoMIP RCP4.5 run due to incongruities between RCP4.5 runs produced for CMIP5 and GeoMIP. Throughout the analyses, differences in MIROC and MIROC-CHEM can be attributed both to differences in initial conditions, since they branch from different control runs, and to the inclusion of the chemistry module. Throughout this paper, we treat them as distinct models even though they are based on the same framework.

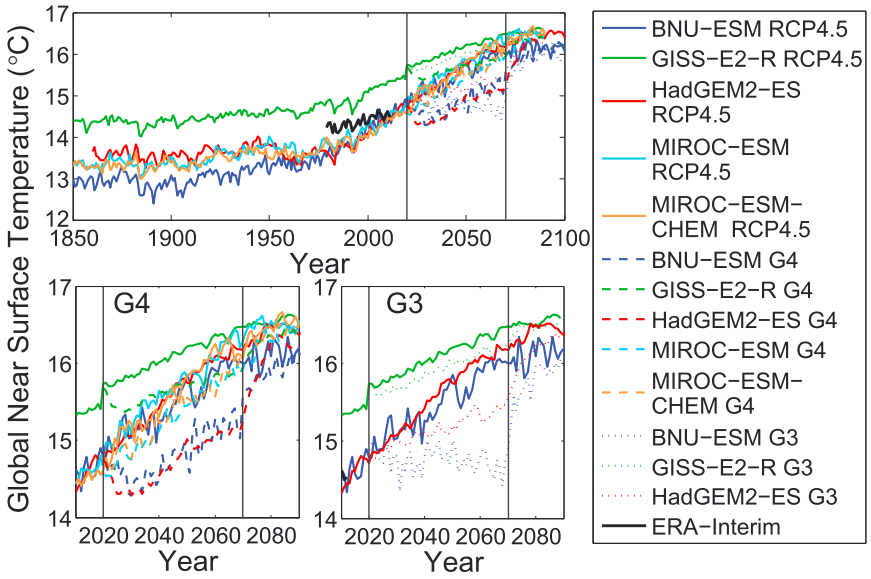

Figure 1. Global annual average temperatures, including land and ocean. GISS-E2-R and HadGEM2-ES curves show the ensemble mean. G4 and G3 are shown separately and zoomed in during the geoengineering period. Solid lines show the control run (RCP4.5), dashed lines the G4 experiments, and dotted lines the G3 experiments. The solid black curve shows the global average ERA-Interim 2 m temperature. Vertical lines indicate the start and finish of the geoengineering experiments at 2020 and 2070.

3. Results

3.1. Temperature

We first compute the global annual average temperature for the RCP4.5 (control run) from 1850 to 2100, G3 and G4 runs from 2020 onward, and the available ERA-Interim 2 m temperature from 1979 to present (Figure 1). The rate of warming in RCP4.5 from 2020 to 2070 averaged over all five models is 0.03 K/a. With the exception of BNU-ESM G3, global temperatures in G3 and G4 are unable to plateau despite sulfate aerosol injections from 2020 to 2070; instead, they show an average increasing trend of 0.01 K/a (G3) and 0.02 K/a (G4), although some individual models still reach rates up to 0.03 K/a. The cooling response to G4 is initially strong, but by 2030, temperatures begin to increase again as the offset from the RCP4.5 run stabilizes with the formation of a stable stratospheric cloud and allows for the slower ocean responses to occur. G3 shows more modest initial cooling and generally less absolute decrease in temperature than G4 compared to RCP4.5.

We next analyze the near surface June-July-August (JJA) Arctic average temperatures, as ice and snow melt are closely related to summer temperatures [*Moore et al.*, 2013] (Figure 2). In the historical period, differences in preferred temperature state between the models are evident; BNU-ESM temperature is roughly 3.5°C colder than the rest of the models pre-2020. As *Berdahl and Robock* [2013] discussed, this has important implications for regions where temperature is near the freezing point, where the change of state of water can induce important climate feedback. In subsequent sections, we will show that this impacts the amount of snow and ice produced in the models. In the G3 and G4 experiments, all models show a decrease in temperature relative to the control run beginning in 2020. In general, the geoengineering runs parallel the warming in the RCP4.5 cases for 2020–2070, albeit at a lower absolute temperature. The average 2020–2070 rate of warming for RCP4.5 is 0.04 K/a, while it is 0.03 K/a and 0.01 K/a for G4 and G3, respectively. The termination effect is visible after 2070, where temperatures rebound toward RCP4.5 temperatures. Differences in G3 and G4 are evident throughout the experiment. For example, G4 tends to produce a larger temperature decrease (by design), although in the BNU-ESM model, G3 sustains the largest negative temperature anomalies.

To assess the degree of Arctic amplification, we compute the ratio of Arctic to global warming trends from 2020 to 2070, shown in Table 2, for annual and relevant seasonal (JJA and September-October-November (SON)) averages. Ratios greater than 1 imply that the Arctic is warming at a faster rate than the global average, i.e., Arctic amplification. In all cases except BNU-ESM G3, there is an amplified warming in the Arctic. In the BNU-ESM G3 cases, denoted with an asterisk in Table 2, there is amplified cooling. The ratio in the BNU-ESM

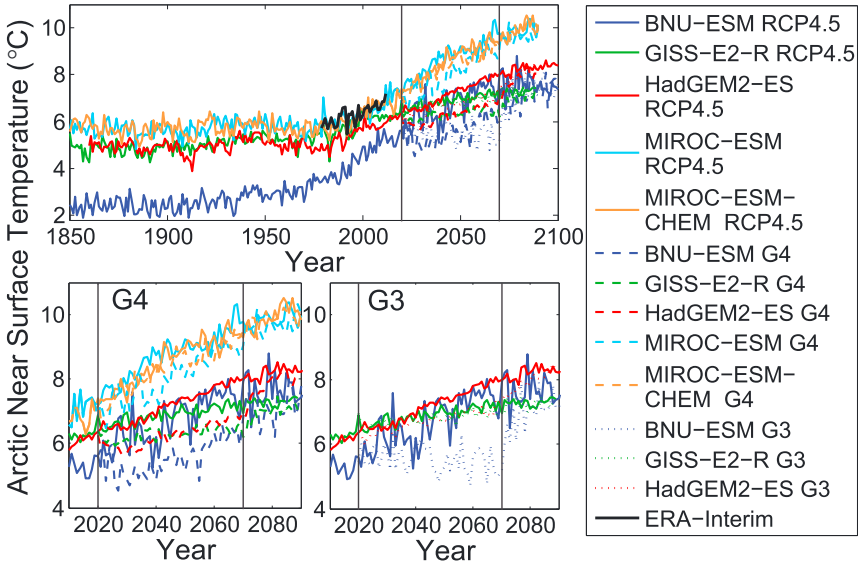

Figure 2. June-July-August (JJA) average temperature for Arctic (north of 60°N), including land and ocean. GISS-E2-R and HadGEM2-ES curves show the ensemble mean. G4 and G3 are shown separately and zoomed in during the geoengineering period. Solid lines show the control run (RCP4.5), dashed lines the G4 experiments, and dotted lines the G3 experiments. The solid black curve shows the ERA-Interim 2 m temperature result for the Arctic (60–90°N). Vertical lines indicate the start and finish of the geoengineering experiments at 2020 and 2070.

G3 annual average case is very large (5.8) since the global mean trend is very near zero so even small differences in the slope produce a large ratio. Results from this analysis suggest that Arctic amplification is a persistent feature in all of the models and experiments, an effect that is stronger in SON than in JJA. The stronger effect in fall than summer is consistent with the expectation of less sea ice, more open water, and the consequent warming of the lower Arctic troposphere, and with our previous understanding of winter Arctic amplification due to sea ice-thermal inertia feedback [*Robock*, 1983]. This also shows that in these geoengineering experiments, the Arctic warms faster than the global average, consistent with previous geoengineering studies [*Lunt et al.*, 2008; *Govindasamy and Caldeira*, 2000; *Matthews and Caldeira*, 2007; *Kravitz et al.*, 2013].

Figures 3 and 4 show the spatial distribution of temperature trends from 2030 to 2070 (beginning in 2030 so that we do not include immediate cooling from sudden implementation of sulfate loading) and 2070 to 2090, the period of rebound after geoengineering ceases, for each model. The rates of warming in both periods show large spatial variability, particularly in the geoengineering experiments. The BNU-ESM and HadGEM2-ES models show a weaker warming in the G3 experiment than the G4 experiment for 2030–2070. All three G3 models show very slight midlatitude warming, likely contributing to the global average temperature increases despite geoengineering. After the SRM forcing has ceased, the strong rebound toward warmer temperatures from 2070 to 2090, which reach up to 0.2 K/a in some locations, is evident in Figure 4, although again the rates are highly spatially variable.

Table 2. Ratio of Arctic (60–90°N) to Global Average Temperature Trends for the Annual Average, June-July-August (JJA) and September-October-November (SON) From 2020 to 2070[a]

	Annual Average			JJA Average			SON Average		
MODEL	RCP4.5	G4	G3	RCP4.5	G4	G3	RCP4.5	G4	G3
BNU-ESM	2.5	2.2	5.8*	1.5	1.5	3.0*	3.1	3.3	4.3*
GISS-E2-R	1.3	1.1	1.2	0.9	0.8	0.6	1.7	1.6	1.7
HadGEM2-ES	2.5	2.9	3.0	1.3	1.4	1.5	2.7	3.2	3.2
MIROC-ESM	2.3	2.3	n/a	1.6	1.5	n/a	2.3	2.7	n/a
MIROC-ESM-CHEM	2.2	2.5	n/a	1.5	1.6	n/a	2.3	2.7	n/a
Average	2.2	2.2	3.4	1.4	1.4	1.7	2.4	2.7	3.1

[a]Values equal to 1 indicate identical rates of warming and values greater than 1 indicate Arctic amplification. Asterisks in BNU-ESM G3 denote negative temperature trends in the Arctic and global average temperatures. Results for MIROC-ESM and MIROC-ESM-CHEM in the G3 experiments are unavailable as of this publication. All cases of Arctic amplification are statistically significant.

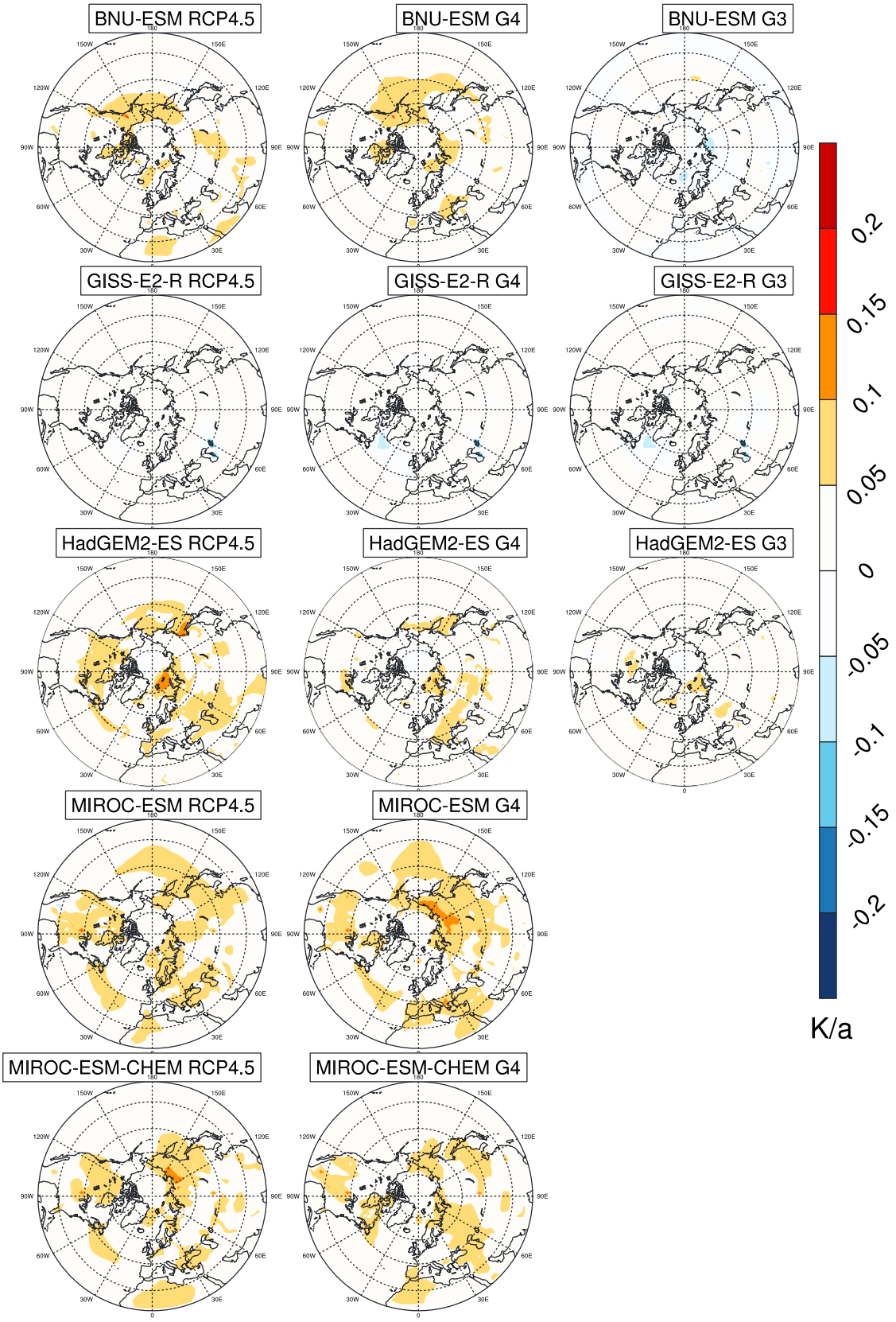

Figure 3. JJA temperature trend from 2030 to 2070 for RCP4.5, G3, and G4 simulations. The rate of warming is generally similar in the geoengineering runs to that in the control runs, although the absolute temperatures are slightly cooler (Figure 2).

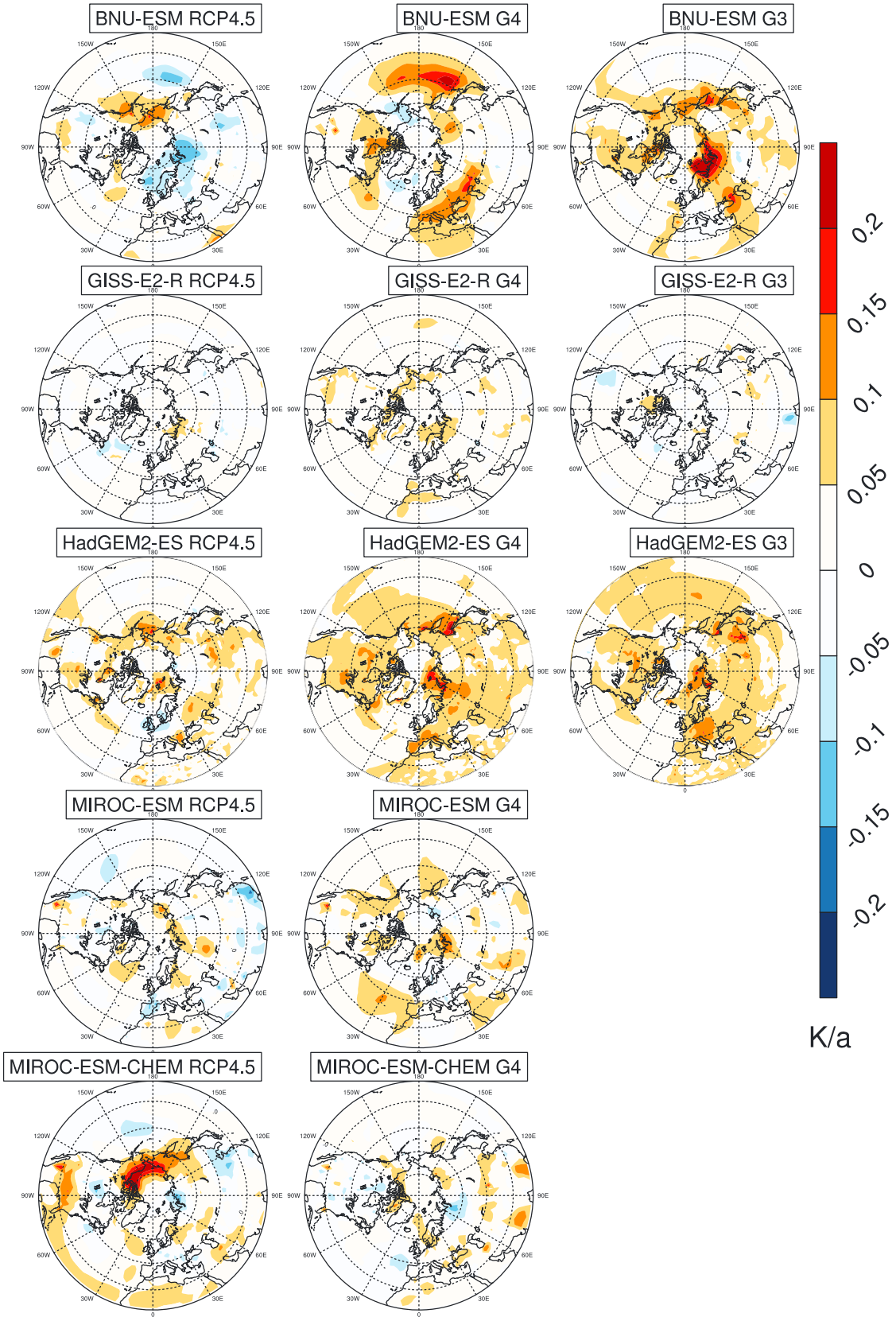

Figure 4. JJA temperature trend from 2070 to 2090 (two decades of recovery after geoengineering) for RCP4.5, G3 and G4 simulations. The rate of warming is generally faster in the geoengineering runs than it is in the control run signifying a fast rebound of temperatures.

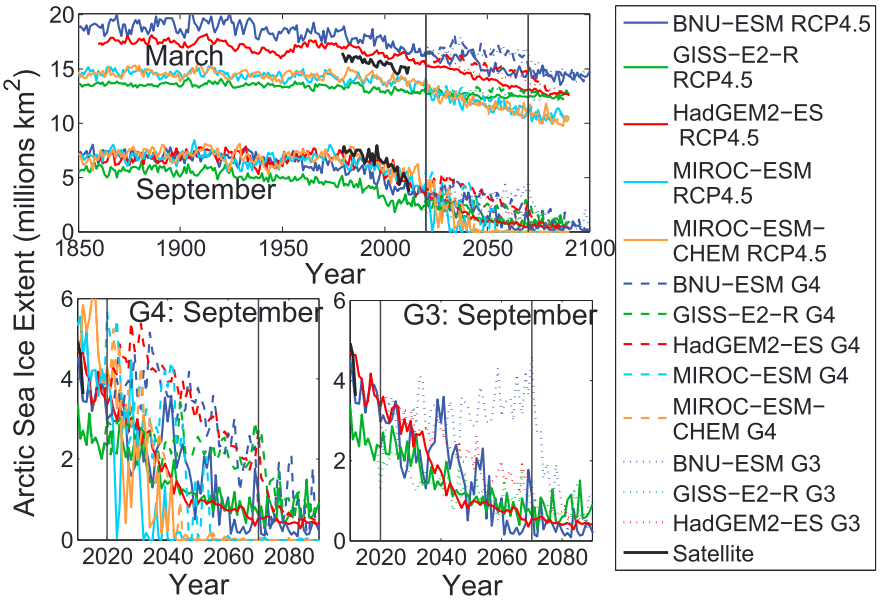

Figure 5. Historical and projected maximum (March) and minimum (September) annual sea ice extent for all available models of the G3 and G4 simulations and satellite observations from 1979 to 2012. Results for G4 and G3 are shown zoomed in for the period 2010 to 2090. Solid lines show the control RCP4.5 run, dashed lines the G4 runs, and dotted lines the G3 runs. MIROC-ESM and MIROC-ESM-CHEM models lose multiyear sea ice before 2050, and the other models approach total sea ice loss by the end of the 21st century, even with geoengineering implemented. Vertical lines denote the beginning and end of the geoengineering experiments (2020–2070).

3.2. Sea Ice

Figures 5–9 analyze the response of the Arctic sea ice extent to the G3 and G4 experiments. Figure 5 shows the sea ice extent over time for March (maximum annual extent) and September (minimum annual extent). The BNU-ESM model simulates the highest sea ice extents on average, consistent with it being the coldest model in Arctic summers.

March sea ice extent is increased compared to the control run during the geoengineering run, although when the sulfate injection is discontinued, the ice extent falls back to RCP4.5 levels within 10 years. All-model average rates of March sea ice loss from 2020 to 2070 in RCP4.5 are 4×10^4 km^2/a, whereas they are 3×10^4 km^2/a and 1×10^4 km^2/a for G4 and G3, respectively. September sea ice extent increases under G3 and G4, although there is still a negative trend overall. All-model average rates of September sea ice loss for 2020–2070 in RCP4.5 are 5×10^4 km^2/a, whereas for G4 and G3 they are 4×10^4 km^2/a and 1×10^4 km^2/a, respectively. These September rates do not include MIROC-ESM or MIROC-ESM-CHEM since those two models reach zero sea ice extent by 2060. In the case of the MIROC-ESM and MIROC-ESM-CHEM models, total loss of minimum annual ice occurs before 2060 despite geoengineering efforts. In all cases the minimum extents fall back to RCP4.5 levels within about 10 years after sulfate loading ceases in 2070, leaving minimal, if any, September ice extent by 2090.

The differences between RCP4.5 and the geoengineering experiments are shown in Figure 6 for March and September. These show clear changes to sea ice extent as a result of geoengineering. In all models, an increase in sea ice extent compared to the control run is visible from 2020 to 2070 for both March and September. The changes in March extent are not as strong, partly because the aerosols will have more effect during summer when the sun is shining in the Arctic. Changes to circulation, meridional heat flux, and clouds could also play a part in the differences in response between March and September. Despite the apparent increases in ice extent as a result of geoengineering compared to the control run, ice extents still decrease overall during geoengineering (Figure 5). Figure 6 also emphasizes the strong termination effect, as ice extents fall to RCP4.5 levels often in less than a decade after 2070 as sulfate aerosol concentrations decay and high CO_2 concentrations begin to dominate the radiative balance.

Figure 7 shows maps of the average September sea ice extent boundaries, both from RCP4.5 for the period before geoengineering (2010–2019) and the last 10 years of geoengineering (2060–2069) for the RCP4.5, G4,

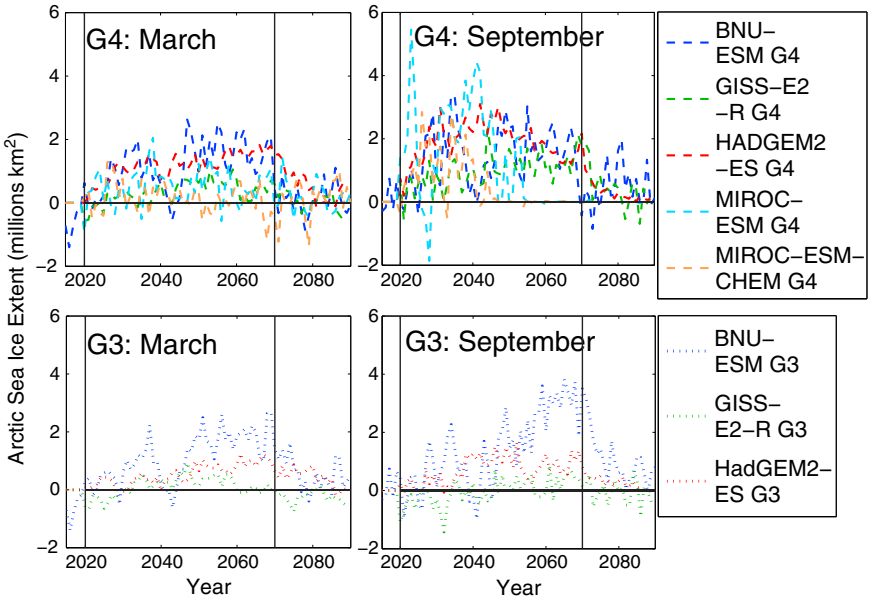

Figure 6. Difference of Arctic sea ice extent between experiment run and control (RCP4.5) for maximum (March) and minimum (September). Dashed lines show G4 experiments; dotted lines show G3. Most models show that the G3 and G4 maintain more sea ice than the control run, but this quickly plummets back to control levels after geoengineering ceases at 2070.

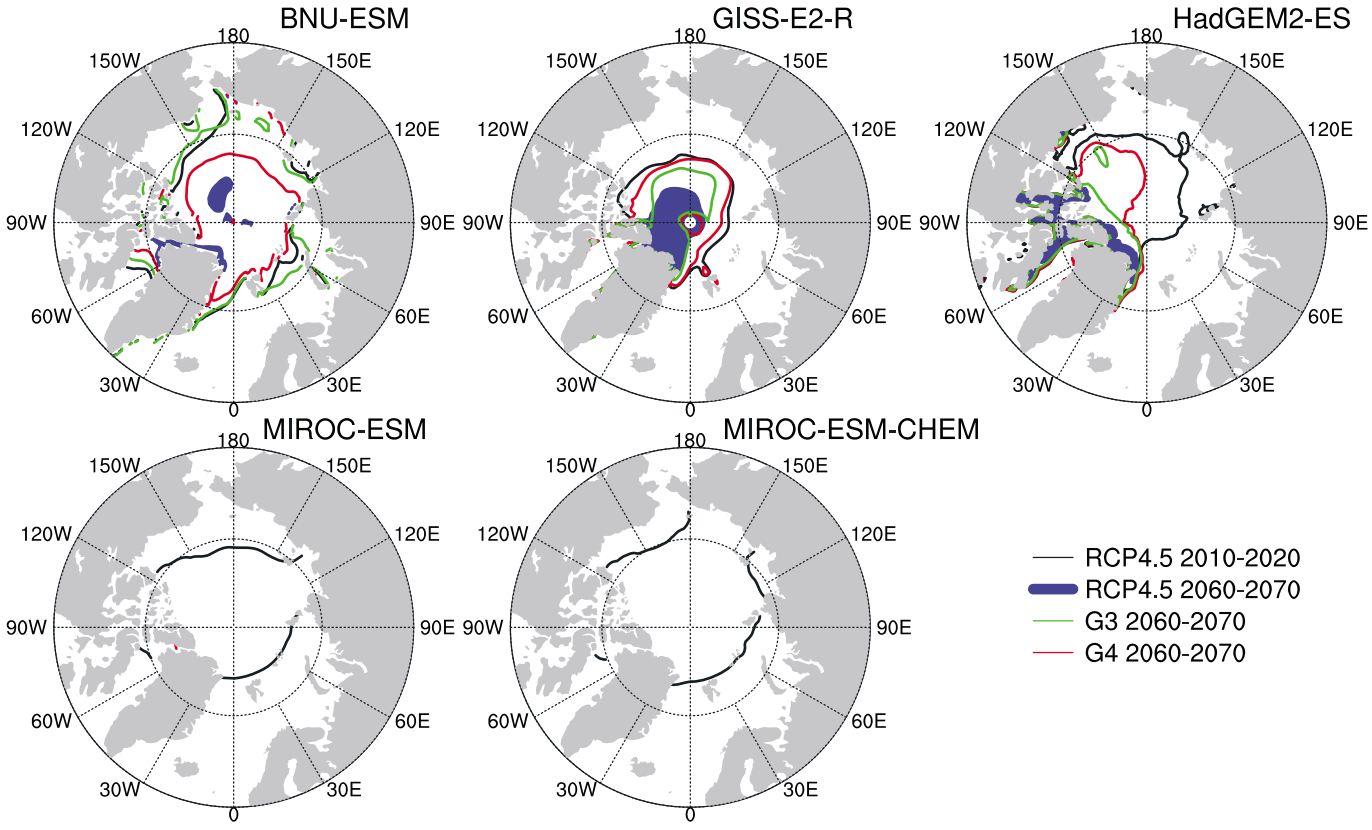

Figure 7. Mean September (minimum) sea ice extent in the RCP4.5 simulation before geoengineering begins (2010–2020, in black) and from 2060 to 2070 in the RCP4.5 (blue filled), G4 (red), and G3 (green) scenarios. MIROC-ESM and MIROC-ESM-CHEM melt virtually all ice by 2060–2070 regardless of the cooling by geoengineering.

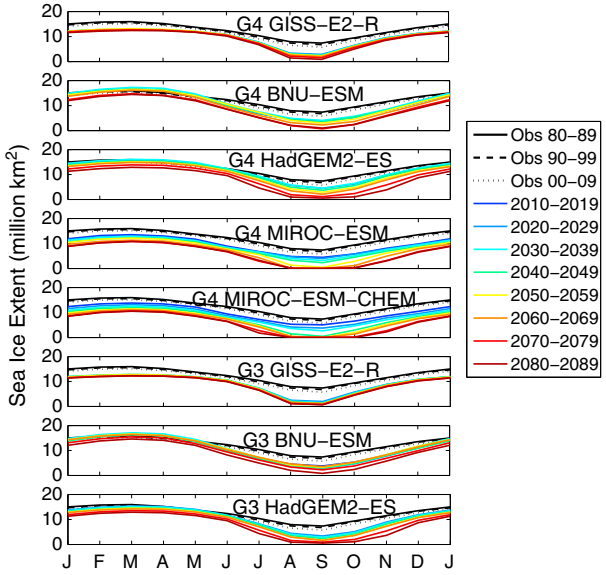

Figure 8. Sea ice extent for G4 and G3 simulations for decadal intervals. The control run is not removed. Extent is defined as grid cells covered by more than 15% ice. Most models show progressively decreasing sea ice area from 2020 to 2090 and exhibit a lengthening of the melt season.

and G3 experiments. The ability of G3 and G4 to maintain an expanded minimum sea ice state is evident in the BNU-ESM and GISS-E2-R models. In BNU-ESM, the G3 simulation sustains more ice than the G4, whereas the opposite is true for GISS-E2-R and HadGEM2-ES. Neither MIROC-ESM nor MIROC-ESM-CHEM retain significant amounts of ice in any of the experiments for the 2060–2070 period. Table 3 outlines how much September sea ice loss was prevented by the geoengineering experiments on average for 2060–2069 as compared to the control run average for 2010–2019. During the last decade of geoengineering (2060–2069), BNU-ESM-G3 and GISS-E2-R G4 prevented the loss of more than 50% of the sea ice as compared to their respective RCP4.5 runs. For all other models and scenarios the values were below 14%, suggesting weak efficacy of preventing sea ice loss. We suspect that part of the intermodel variation in the success of September ice loss prevention is related to the absolute JJA Arctic temperatures (Figure 2). That is, warmer models like the MIROC models lose sea ice completely regardless of geoengineering, whereas colder models such as GISS-E2-R and BNU-ESM tend to be more successful at retaining September sea ice extents.

We also analyzed decadal changes of sea ice extent (Figure 8). All models show a steady decrease in ice extent across all months for the entire experimental period, despite cooling efforts in both G3 and G4. In MIROC-ESM and MIROC-ESM-CHEM, it is clear that summer ice effectively disappears midway through the 21st century. Another noteworthy feature of Figure 8 is the lengthening of the melt season with time. In the geoengineering simulations, as the decades progress, ice begins to melt faster and earlier and requires more time to rebuild into the fall and winter. Very similar results are found for sea ice volume, shown in Figure 9. MIROC-ESM and MIROC-ESM-CHEM sea ice volume is underestimated at the beginning of the 21st century and decreases rapidly, likely contributing to the weakness of the sea ice response to G4 forcing.

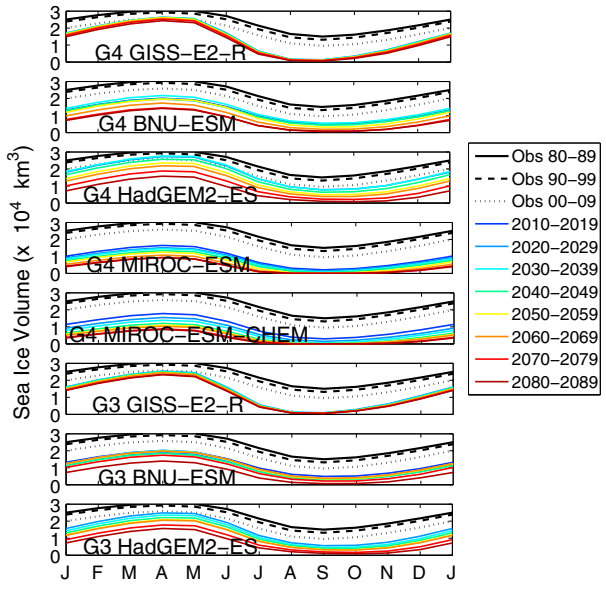

Figure 9. Decadally-averaged sea ice volume from 2010 to 2090. The control has not been removed. Melt seasons last longer, and ice volume approaches zero as the decades progress. Average 2005–2012 observed values are shown in the black curve. Sea ice volume observations are calculated using the Pan-Arctic Ice Ocean Modeling and Assimilation System [*Zhang and Rothrock*, 2003] developed at Applied Physics Laboratory/Polar Science Center (APL/PSC).

3.3. Snow Response

We analyze the historical and projected spring (April–June) Northern Hemisphere snow cover extent. Snow is typically limited to the Arctic during these months [*Derksen and Brown*, 2012]. The HadGEM2-ES model unfortunately did not output the fractional snow cover variable, so our

Table 3. Percentage of September Sea Ice Loss that Was Prevented by the Geoengineering Experiments During the Last Decade of Sulfate Aerosol Loading (2060–2069) as Compared to the Control Run Average From 2010 to 2019[a]

Model	G4 Experiment	G3 Experiment
BNU-ESM	7.7 %	60.8 %
GISS-E2-R	54.7 %	3.5 %
HadGEM2-ES	13.4 %	4.9 %
MIROC-ESM	0.2 %	n/a
MIROC-ESM-CHEM	0.0 %	n/a

[a]These are computed as $(G_f - C_f)/(C_i - C_f)$ where the subscripts *f* and *i* denote the final (2060–2069) and initial (2010–2019) period, respectively, and *G* and *C* refer to the geoengineering and control runs.

analyses of snow cover are limited to the remaining four models.

Figure 10 shows the April, May, and June snow extent, based on a 50% fractional cover threshold. Similar to the results for sea ice, the relatively cold BNU-ESM model generates the greatest snow cover area of all models available. Snow extents decrease beginning around the turn of the 21st century and are projected to continue decreasing through to 2100 in the RCP4.5 simulations. This qualitative pattern is consistent among models and among all spring months. The G3 and G4 experiments generally show an increase in snow cover compared to the control run during the 2020–2070 period in April, May, and June, although the results show interannual variability. The models range in their responsiveness to sulfate aerosol injection. MIROC-ESM and MIROC-ESM-CHEM show the least response of snow cover in all months, while the BNU-ESM model tends to respond with the largest snow cover changes of all the models. The GISS-E2-R model shows very little response in the

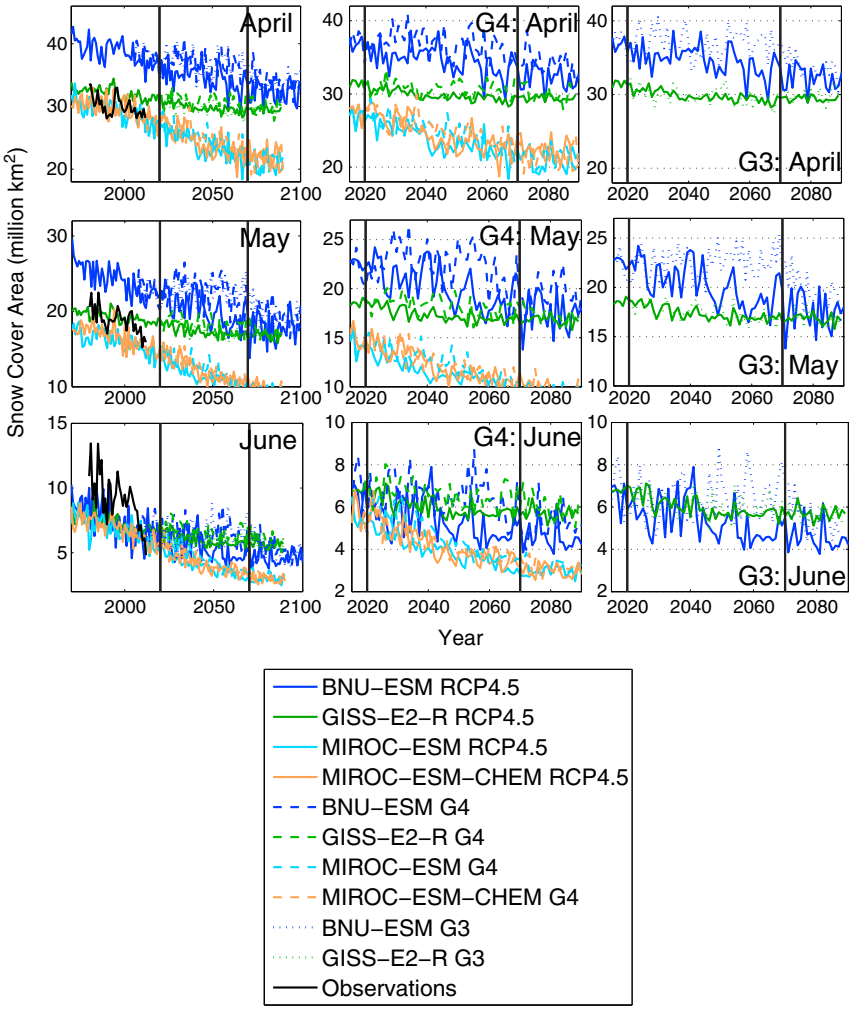

Figure 10. Spring (April–June) snow cover extent (> 50% coverage) for the Northern Hemisphere. During these months, snow extent is mostly limited to the Arctic. HadGEM2-ES fractional snow cover data are not available. Snow extent is increased during the G3 and G4 experiments, most for BNU-ESM, followed by GISS-E2-R and MIROC-ESM/MIROC-ESM-CHEM which show only slight snow extent increases. After 2070, snow extents in the G3 and G4 experiments decrease quickly back to RCP4.5 values.

Table 4. Change of Snow Extent From 2020 to 2070[a]

	April			May			June		
MODEL	RCP4.5	G4	G3	RCP4.5	G4	G3	RCP4.5	G4	G3
BNU-ESM	−52	−47	6	−87	−52	25	−19	−15	14
GISS-E2-R	−49	−7	−41	−23	−17	−21	−19	−11	−12
MIROC-ESM	−114	−103	n/a	−81	−77	n/a	−39	−55	n/a
MIROC-ESM-CHEM	−126	−107	n/a	−88	−85	n/a	−43	−40	n/a
Average	−85	−66	−17	−70	−58	2	−30	−30	1

[a]Units are thousands of square kilometers ($\times 10^3$ km^2).

G3 experiment in terms of snow expansion. Similar to the sea ice and temperature results, after sulfate aerosol injection is halted, snow extents decrease back to RCP4.5 levels in less than a decade.

Table 4 shows the rates of change of snow extent cover for 2020–2070 in all simulations for April, May, and June. In the RCP4.5 runs, snow loss rates are generally highest in April, followed by May and June. In all geoengineering cases, the rate of snow loss is slowed compared to the RCP4.5 run. All G4 and G3 simulations still show a decreasing snow extent trend, except for BNU-ESM G3 which effectively levels off or increases snow extents over time. MIROC-ESM and MIROC-ESM-CHEM models show few effects on reducing snow loss, similar to their performance with sea ice.

4. Summary

We find positive temperature trends during the geoengineering period from 2020 to 2070. The mean rate of warming in RCP4.5 from 2020 to 2070 is 0.03 K/a, while it is 0.02 K/a for G4 and 0.01 K/a in G3. Cooling is strong and immediate in G4 at 2020, but by 2030, temperatures begin to increase again as CO_2 levels dominate the 5 Tg sulfate aerosol/a inputs. G3 shows more modest initial cooling, and generally less absolute decrease in temperature than G4 compared to RCP4.5.

Arctic summer temperatures track the patterns of global annual averages. In general, the JJA temperatures show the same warming trend as the RCP4.5 cases from 2020 to 2070 but are offset relative to the RCP4.5 cases by a roughly constant negative value. We find that there is still a persistent warming trend underlying the 50 year period of active geoengineering. The average 2020–2070 rate of warming for RCP4.5 is 0.04 K/a, whereas it is 0.03 K/a and 0.01 K/a for G4 and G3, respectively. Rates of warming are spatially and temporally variable, and as a consequence, we suggest that actual stratospheric injection of SO_2 in the real world would produce variable outcomes. Further, the rebound to RCP4.5 temperatures after geoengineering is abruptly discontinued produces extreme rates of warming in certain regions, up to 0.2 K/a. We find statistically significant Arctic amplification in both the RCP4.5 and geoengineering experiments, predominantly in the form of amplified warming, but in the case of BNU-ESM G3, amplified Arctic cooling.

The G3 and G4 GeoMIP simulations indicate disagreement between the models regarding the response of Arctic sea ice to sulfate geoengineering. In two of the five models, the complete disappearance of September sea ice is not avoided by sulfate aerosol injection in the G4 experiment. In the models that do retain sea ice, G3 and G4 produce differing outcomes for different models; neither experiment is obviously more effective at retaining ice. Sea ice extents follow a negative trend through the geoengineering period despite sulfate aerosol injection: -5×10^4 km^2/a for RCP4.5, -4×10^4 km^2/a for G4, and -1×10^4 km^2/a for G3. The percentage of sea ice loss that was prevented by the geoengineering experiments during the last decade of sulfate aerosol loading (2060–2069) as compared to the control run average for 2010–2019 reached above 50% in the BNU-ESM G3 and GISS-E2-R G4 scenarios, but in all other scenarios, the values were below 14% (Table 3). Models with warmer summer Arctic temperatures (MIROC-ESM and MIROC-ESM-CHEM) do not maintain September sea ice, while colder models (BNU-ESM and GISS-E2-R) are most successful at keeping September ice. No models are capable of retaining 2020 September sea ice extents throughout the entire geoengineering period. Generally, there is a decrease in ice extent in all months and a lengthening of the melt season in G3 and G4.

Post-2070 ice extents collapse back to RCP4.5 levels within roughly 10 years. Results from snow cover are commensurate with the ice and temperature responses. Except for BNU-ESM G3, spring snow cover areas are temporarily increased during the geoengineering years, again superimposed on a negative trend, followed by a quick decrease toward RCP4.5 values after 2070.

Despite some cooling, and the general ability of the models to retain greater areas of snow and ice than the RCP4.5 run, the degree of these effects are variable from year to year, model to model and experiment to experiment. Even then, ice and snow continue to melt and temperatures continue to rise globally, with amplification in the Arctic. Given the termination effect, if warming is inevitable, slow rates are preferable to quick rates since drastic changes will have much more devastating impacts [*Parry et al*., 2007]. Beyond the physical consequences of global warming such as ice and snow loss are the implications as a result of these changes, such as global sea level rise, ice sheet mass balance, water resources, wildlife habitat loss, and human activities in the Arctic.

5. Discussion and Conclusions

We show that SRM in the form of sulfate aerosol loading in the G3 and G4 experiments is successful at producing some global annual average temperature cooling. With the exception of BNU-ESM G3, the global average temperatures in G3 do not remain at the level of 2020 values. This is in contrast to the results found for G1 [*Kravitz et al*., 2013; *Moore et al*., 2013] and G2 [*Jones et al*., 2013], where global average temperatures and sea ice are generally kept constant by SRM efforts. The difference between G1 and G2 on the one hand, and G3 on the other, is that G1 and G2 are very artificial, starting with a balanced control run. G3 branches from a realistic global warming simulation, so even though top of atmosphere net radiation is kept at 2020 values, global warming still occurs. The lag in ocean response to the initial forcing produces a small, but nonnegligible, continued warming. With Arctic amplification, this continued warming is felt even more strongly in the regions with snow and sea ice.

This means that, if the goal of a geoengineering implementation were to stop global warming, or to stop snow and sea ice melting and keep them at the levels that existed at the time of the initiation of geoengineering, a global average negative net radiative forcing would be necessary. If the goal were to restore snow and sea ice to their values in a previous year, an even larger negative forcing would have to be imposed, such as in G4, but it would have to increase over time in the absence of mitigation. This would impose an even larger termination effect than shown here, should society lose the will or means to continue stratospheric aerosol injection.

Acknowledgments

We thank all participants of the Geoengineering Model Intercomparison Project and their model development teams, CLIVAR/WCRP Working Group on Coupled Modeling for endorsing GeoMIP, and the scientists managing the Earth System Grid data nodes who have assisted with making GeoMIP output available. We acknowledge the World Climate Research Programme's Working Group on Coupled Modelling, which is responsible for CMIP, and we thank the climate modeling groups for producing and making available their model output. For CMIP, the U.S. Department of Energy's Program for Climate Model Diagnosis and Intercomparison provides coordinating support and led development of software infrastructure in partnership with the Global Organization for Earth System Science Portals. We thank David Robinson for insightful discussions and the Rutgers University Snow Lab for snow cover data. MB and AR were supported by NSF grants CBET-1240507, AGS-1157525, and ARC-0908834. Some figures were drawn with the NCAR Command Language (NCL, http://dx.doi.org/10.5065/D6WD3XH5). AJ was supported by the Joint DECC/Defra Met Office Hadley Centre Climate Programme (GA01101). SW was supported by SOUSEI program, MEXT, Japan and his simulations were performed using the Earth Simulator. BK is supported by the Fund for Innovative Climate and Energy Research. The Pacific Northwest National Laboratory is operated for the U.S. Department of Energy by Battelle Memorial Institute under contract DE-AC05-76RL01830. Simulations performed by BK were supported by the NASA High-End Computing Program through the NASA Center for Climate Simulation at Goddard Space Flight Center.

References

Ahmed, M., et al. (2013), Continental-scale temperature variability during the past two millennia, *Nat. Geosci.*, *6*, 339–346, doi:10.1038/NGE01797.

Barnes, J. E., and D. J. Hoffman (1997), Lidar measurements of stratospheric aerosol over Mauna Loa Observatory, *Geophys. Res. Lett.*, *24*(15), 1923–1926.

Berdahl, M., and A. Robock (2013), Northern Hemispheric cryosphere response to volcanic eruptions in the Paleoclimate Model Intercomparison Project 3 last millennium simulations, *J. Geophys. Res. Atmos.*, *118*, 12,359–12,370, doi:10.1029/2013JD019914.

Bluth, G. J. S., S. D. Doiron, S. C. Schnetzler, A. J. Krueger, and L. S. Walter (1992), Global tracking of the SO2 clouds from the June, 1991 Mount Pinatubo eruptions, *Geophys. Res. Lett.*, *19*, 151–154, doi:10.1029/91GL02792.

Brown, R. D., and D. A. Robinson (2011), Northern Hemisphere spring snow cover variability and change over 1922–2010 including an assessment of uncertainty, *Cryosphere*, *5*, 219–229, doi:10.5194/tc-5-219-2011.

Callaghan, T. V., et al. (2011), The changing face of Arctic snow cover: A synthesis of observed and projected changes, *AMBIO*, *40*, 17–31, doi:10.1007/s13280-011-0212-y.

Collins, W. J., et al. (2011), Development and evaluation of an Earth-System model – HadGEM2, *Geosci. Model Dev.*, *4*, 1051–1075, doi:10.5194/gmd-4-1051-2011.

Crutzen, P. J. (2006), Albedo enhancements by stratospheric sulfur injections: A contribution to resolve a policy dilemma? An editorial essay, *Clim. Change*, *77*, 211–219.

Dai, Y., et al. (2003), The Common Land Model (CLM), *Bull. Am. Meteorol. Soc.*, *84*, 1013–1023, doi:10.1175/BAMS-84-8-1013.

Dai, Y., R. E. Dickinson, and Y.-P. Wang (2004), A two-big-leaf model for canopy temperature, photosynthesis, and stomatal conductance, *J. Clim.*, *17*, 2281–2299, doi:10.1175/1520-0442(2004)017<2281:ATMFCT>2.0.CO;2.

Dee, D. P., et al. (2011), The ERA-Interim reanalysis: Configuration and performance of the data assimilation system, *Q. J. R. Meteorol. Soc.*, *137*, 553–597, doi:10.1002/qj.828.

Derksen, C., and R. Brown (2012), Spring snow cover extent reductions in the 2008–2012 period exceeding climate model projections, *Geophys. Res. Lett.*, *39*, L19504, doi:10.1029/2012GL053387.

Fetterer, F., K. Knowles, W. Meier, and M. Savoie (2009), *Sea Ice Index*, [Sea Ice Extent], National Snow and Ice Data Center, Boulder, Colo., doi:10.7265/N5QJ7F7W.

Francis, J. A. and S. J. Vavrus (2012), Evidence linking Arctic amplification to extreme weather in mid-latitudes, *Geophys. Res. Lett. 39*, L06801, doi:10.1029/2012GL051000.

Govindasamy, B., and K. Caldeira (2000), Geoengineering Earth's radiation balance to mitigate CO_2-induced climate change, *Geophys. Res. Lett.*, *27*, 2141–2144.

Irvine, P. J., D. J. Lunt, E. J. Stone, and A. Ridgwell (2009), The fate of the Greenland Ice Sheet in a geoengineered, high CO_2 world, *Environ. Res. Lett.*, *4*, doi:10.1088/1748-9326/4/4/045109.

Jones, A., J. Haywood, O. Boucher, B. Kravitz, and A. Robock (2010), Geoengineering by stratospheric SO_2 injection: Results from the Met Office HadGEM2 climate model and comparison with the Goddard Institute for Space Studies ModelE, *Atmos. Chem. Phys.*, *10*, 5999–6006, doi:10.5194/acp-10-5999-2010.

Jones, A., et al. (2013), The impact of abrupt suspension of solar radiation management (termination effect) in experiment G2 of the Geoengineering Model Intercomparison Project (GeoMIP), *J. Geophys. Res. Atmos.*, *118*, 9743–9752, doi:10.1002/jgrd.50762.

Kravitz, B., A. Robock, O. Boucher, H. Schmidt, K. Taylor, G. Stenchikov, and M. Schulz (2011a), The Geoengineering Model Intercomparison Project (GeoMIP), *Atmos. Sci. Lett.*, *12*, 162–167, doi:10.1002/asl.316.

Kravitz, B., A. Robock, O. Boucher, H. Schmidt, K. Taylor, G. Stenchikov, and M. Schulz (2011b), Specifications for GeoMIP experiments G1 through G4. [Available at http://climate.envsci.rutgers.edu/GeoMIP/docs/specificationsG1_G4_v1.0.pdf.]

Kravitz, B., et al. (2013), Climate model response from the Geoengineering Model Intercomparison Project (GeoMIP), *J. Geophys. Res. Atmos.*, *118*, 8320–8332, doi:10.1002/jgrd.50646.

Lane, L., K. Caldeira, R. Chatfield, and S. Langhoff (Eds.) (2007), Workshop report on managing solar radiation, *NASA/CP-20070214558*, 31 pp.

Launder, B., and J. M. T. Thompson (Eds.) (2009), *Geo-Engineering Climate Change: Environmental Necessity or Pandora's Box?*, Cambridge Univ. Press, Cambridge, U. K.

Lenton, T. M., and N. E. Vaughan (2009), The radiative forcing potential of difference climate geoengineering options, *Atmos. Chem. Phys.*, *9*, 5539–5561.

Lunt, D. J., A. Ridgwell, P. J. Valdes, and A. Seale (2008), "Sunshade World": A fully coupled GCM evaluation of the climatic impacts of geoengineering, *Geophys. Res. Lett.*, *35*, L12710, doi:10.1029/2008GL033674.

Matthews, H. D., and K. Caldeira (2007), Transient climate-carbon simulations of planetary geoengineering, *Proc. Natl. Acad. Sci. U. S. A.*, *104*, 9949–9954.

Moore, J. C., et al. (2013), Arctic sea ice and atmospheric circulation under the GeoMIP G1 scenario, *J. Geophys. Res. Atmos.*, doi:10.1002/2013JD021060.

Moss, R. H., et al. (2010), The next generation of scenarios for climate change research and assessment, *Nature*, *463*, 747–756, doi:10.1038/nature08823.

Niemeier, U., H. Schmidt, and C. Timmreck (2011), The dependency of geoengineered sulfate aerosol on the emission strategy, *Atmos. Sci. Lett.*, *12*, 189–194, doi:10.1002/asl.304.

National Snow and Ice Data Center (NSIDC) (2012), Arctic sea ice news and news analysis. [Available at http://nsidc.org/arcticseaicenews/2012/09/arctic-sea-ice-extent-settles-at-record-seasonal-minimum/.]

Parry, M. L., et al. (2007), Technical summary. *Climate Change 2007: Impacts, Adaptation and Vulnerability. Contribution of Working Group II to the Fourth Assessment Report of the Intergovernmental Panel on Climate Change*, pp. 23–78 , Cambridge Univ. Press, Cambridge, U. K.

Rasch, P. J., S. Tilmes, R. P. Turco, A. Robock, L. Oman, C.-C. Chen, G. L. Stenchikov, and R. R. Garcia (2008), An overview of geoengineering of climate using stratospheric sulfate aerosols, *Phil. Trans. R. Soc. A*, *366*, 4007–4037, doi: 10.1098/rsta.2008.0131.

Robock, A. (1983), Ice and snow feedbacks and the latitudinal and seasonal distribution of climate sensitivity, *J. Atmos. Sci.*, *40*, 986–997.

Robock, A. (2000), Volcanic eruptions and climate, *Rev. Geophys.*, *38*, 191–219.

Robock, A., L. Oman, and G. L. Stenchikov (2008), Regional climate responses to geoengineering with tropical and Arctic SO_2 injections, *J. Geophys. Res.*, *113*, D16101, doi:10.1029/2008JD010050.

Robock, A., A. B. Marquardt, B. Kravitz, and G. Stenchikov (2009), The benefits, risks and costs of stratospheric geoengineering, *Geophys. Res. Lett.*, *36*, L19703, doi:10.1029/2009GL039209.

Schaefer, K., T. Zhang, L. Bruhwiler, and A. P. Barrett (2011), Amount and timing of permafrost carbon release in response to climate warming, *Tellus*, *63B*, 165–180, doi:10.1111/j.1600-0889.2011.00527.x.

Schmidt, G. A., et al. (2006), Present-day atmospheric simulations using GISS ModelE: Comparison to in situ, satellite and reanalysis data, *J. Clim.*, *19*, 153–192, doi:10.1175/JCLI3612.1.

Screen, J., and I. Simmonds (2010), The central role of diminishing sea ice in recent Arctic temperature amplification, *Nature*, *464*, 1334–1337, doi:10.1038/nature09051.

Serreze, M. C., and J. A. Francis (2006), The Arctic amplification debate, *Clim. Change*, *76*, 241–264.

Serreze, M. C., M. M. Holland, and J. Stroeve (2007), Perspectives on the Arctic's shrinking ice cover, *Science*, *315*, 1533–1536.

Serreze, M. C., A. P. Barrett, J. C. Stroeve, D. N. Kindig, and M. M. Holland (2009), The emergence of surface-based Arctic amplification, *Cryosphere*, *3*, 11–19.

Shepherd, J., et al. (2009), Geoengineering the climate: Science, governance and uncertainty, Royal Society Policy document 10/09. (Royal Society, London), 82 pp.

Solomon, S., D. Qin, M. Manning, Z. Chen, M. Marquis, K. B. Averyt, M. Tignor, and H. L. Miller (Eds.) (2007), *Climate Change 2007: The Physical Science Basis*, Cambridge Univ. Press, United Kingdom and New York.

Stroeve, J. C., V. Kattsov, A. Barrett, M. Serreze, T. Pavlova, M. Holland and W. N. Meier (2012), Trends in Arctic sea ice extent from CMIP5, CMIP3 and observations. *Geophys. Res. Lett. 39*, L19502, doi: 10.1029/2012GL052676.

Tilmes, S., R. Muller, and R. Salawitch (2008), The sensitivity of polar ozone depletion to proposed geoengineering schemes, *Science*, *320*, 1201–1204, doi:10.1126/science.1153966.

Tingley, M. P., and P. Huybers (2013), Recent temperature extremes at high northern latitudes unprecedented in the past 600 years, *Nature*, *496*, 201–205, doi:10.1038/nature11969.

Uppala, S. M., et al. (2005), The ERA-40 reanalysis, *Q. J. R. Meteorol. Soc.*, *131*, 2961–3012, doi:10.1256/qj.04.176.

Wang, M., and J. E. Overland (2012), A sea ice free summer Arctic within 30 years—An update from the CMIP5 models, *Geophys. Res. Lett.*, *39*, L18501, doi:10.1029/2012GL052868.

Watanabe, S., et al. (2011), MIROC-ESM 2010: Model description and basic results of CMIP5-20c3m experiments, *Geosci. Model Dev.*, *4*, 845–872, doi:10.5194/gmd-4-845-2011.

Wigley, T. M. L. (2006), A combined mitigation/geoengineering approach to climate stabilization, *Science*, *314*, 452–454, doi:10.1126/science.

Zhang, J., and D. A. Rothrock (2003), Modeling global sea ice with a thickness and enthalpy distribution model in generalized curvilinear coordinates, *Mon. Wea. Rev.*, *131*, 845–861, doi:10.1175/1520-0493(2003)131<0845:MGSIWA>2.0.CO;2.